International Journal of Heat and Mass Transfer 82 (2015) 109–116

Contents lists available at ScienceDirect

International Journal of Heat and Mass Transfer

journal homepage: www.elsevier.com/locate/ijhmt

Enhanced pool-boiling heat transfer and critical heat flux on femtosecond laser processed stainless steel surfaces

Corey M. Kruse [a], Troy Anderson [b], Chris Wilson [b], Craig Zuhlke [b], Dennis Alexander [b], George Gogos [a], Sidy Ndao [a,*]

[a] Mechanical and Materials Engineering, University of Nebraska – Lincoln, Lincoln, NE 68588, USA
[b] Electrical Engineering, University of Nebraska – Lincoln, Lincoln, NE 68588, USA

ARTICLE INFO

Article history:
Received 18 July 2014
Received in revised form 6 October 2014
Accepted 6 November 2014

Keywords:
Pool boiling
Critical heat flux
Femtosecond laser surface processing
Heat transfer coefficients
Metallic enhanced heat transfer surfaces

ABSTRACT

In this paper, we present an experimental investigation of pool boiling heat transfer on multiscale (micro/nano) functionalized metallic surfaces. Heat transfer enhancement in metallic surfaces is very important for large scale high heat flux applications like in the nuclear power industry. The multiscale structures were fabricated via a femtosecond laser surface process (FLSP) technique, which forms self-organized mound-like microstructures covered by layers of nanoparticles. Using a pool boiling experimental setup with deionized water as the working fluid, both the heat transfer coefficients and critical heat flux were investigated. A polished reference sample was found to have a critical heat flux of 91 W/cm^2 at 40 °C of superheat and a maximum heat transfer coefficient of 23,000 W/m^2 K. The processed samples were found to have a maximum critical heat flux of 142 W/cm^2 at 29 °C and a maximum heat transfer coefficient of 67,400 W/m^2 K. It was found that the enhancement of the critical heat flux was directly related to the wetting and wicking ability of the surface which acts to replenish the evaporating liquid and delay critical heat flux. The heat transfer coefficients were also found to increase when the surface area ratio was increased as well as the microstructure peak-to-valley height. Enhanced nucleate boiling is the main heat transfer mechanism, and is attributed to an increase in surface area and nucleation site density.

© 2014 Elsevier Ltd. All rights reserved.

1. Introduction

Two-phase heat transfer on micro and nanostructured surfaces has attracted much research interest in recent time [1]. This is due to the observed high heat transfer coefficients and critical heat flux. Most pool boiling experiments for enhanced heat transfer have been conducted on micro and nanostructured surfaces fabricated using complex fabrication techniques such as etching and thin film depositions carried out in highly controlled environments (i.e., cleanroom). These techniques have been very effective at increasing the critical heat flux (CHF) as well as heat transfer coefficients (HTC) through a combination of increased surface roughness, wettability, and porosity. These microfabrication techniques have been used to create very organized arrays of microstructures ranging from pillars to microchannels and have demonstrated CHF values of 100–200 W/cm^2 [2–4] for pillars and 100 W/cm^2 [5] for microchannels. When nanoscale features are added to these microstructures, the critical heat flux can be further increased. Values as high as 230 W/cm^2 [2] have been reported, showing that hierarchical structures can significantly increase the performance of heat transfer surfaces. In addition to surface microstructuring, it has also been shown that varying surface chemistry, such as provided by a combination or network of hydrophilic and hydrophobic areas on a surface can significantly enhance the heat transfer performance as well. Hydrophobic surfaces lead to easily activated nucleation sites, a decrease in the onset of nucleate boiling, and possible increase in heat transfer coefficients, but result in a much lower critical heat flux [6–8]. Hydrophilic surfaces meanwhile delay the formation of a stable vapor layer from forming and thus delaying the critical heat flux. A combination of these types of surfaces allows for an optimization of the heat transfer performance [6–9].

In addition to microstructures, silicon and copper nanowire coatings have also been used for two-phase heat transfer enhancement. These types of surfaces have been shown to produce CHF values in the range of 120–250 W/cm^2 [10–12]. Such CHF enhancements have been attributed to high nucleation site density, superhydrophilicity, and enhanced capillary wicking.

All of the previously mentioned experimental results were obtained with a heat transfer surface comprised of a silicon base

* Corresponding author.
E-mail address: sndao2@unl.edu (S. Ndao).

http://dx.doi.org/10.1016/j.ijheatmasstransfer.2014.11.023
0017-9310/© 2014 Elsevier Ltd. All rights reserved.

material which is advantageous in small applications such as electronics cooling. These types of surface enhancement techniques are, however, not practical for applications which require metallic heat transfer surfaces and much larger areas.

The enhancement of heat transfer using metallic surfaces is especially important for large scale operations like in the nuclear power plant industry. Some work has been done to enhance heat transfer with a metallic base surface using techniques such as anodizing processes or material deposition to achieve the desired micro/nanostructures; however these techniques are often applicable to a limited type of base material. For zircaloy-4 (commonly used in the nuclear industry), it has been shown that the critical heat flux can be increased up to about 200 W/cm^2 by using a simple anodizing method [13,14]. This work resulted in a very good enhancement of the critical heat flux but no real enhancement of the heat transfer coefficients. In other studies, alumina was deposited onto platinum using atomic layer deposition [15] and zinc oxide was deposited onto copper and aluminum surfaces in order to enhance two-phase heat transfer [16]. The alumina deposition on platinum resulted in a CHF of around 120 W/cm^2 while the zinc oxide covered surface only reached maximum heat fluxes of about 80 W/cm^2. Both techniques resulted in an enhancement of the heat transfer coefficients. Anodizing has also been applied to aluminum surfaces [17] to induce a nanoporous layer. This resulted in a CHF of around 90 W/cm^2 but minimal heat transfer coefficient enhancement. Other enhancement techniques have also been applied to metallic surfaces such as copper. Surface sintering and the addition of nanorods have been shown to increase the heat transfer coefficients of both types of surfaces but with no major enhancement of the critical heat flux [18,19].

The present study focuses on the pool boiling heat transfer performance of 304 stainless steel multiscale micro/nano-structures fabricated via femtosecond laser surface processing (FLSP). FLSP uses an ultra-fast laser to ablate and form a self-organized array of mound like microstructures with a nanoparticle layer on nearly any metallic surface [20]. This method is a one step process that has the advantage of being able to process nearly any size of area with a very high precision.

2. Experimental procedures

2.1. Surface processing and characterization

The impact of multiscale surface structures on the heat transfer coefficient and critical heat flux of stainless steel was investigated through the characterization of four FLSP-generated samples with a polished sample as a control. Structured surfaces fabricated via FLSP are characterized by a series of self-organized quasi-periodic microstructure covered by a layer of nanoparticles [21–27]. Specific physical characteristics including the peak to valley height, microstructure spacing, and nanoparticle layer thickness are a function of the laser fluence and number of incident laser pulses. A schematic of the FLSP setup is shown in Fig. 1. The fabrication laser was a Ti:Sapphire (Spitfire, Spectra Physics) that produced ~50 femtosecond pulses with a central wavelength of 800 nm at a 1 kHz repetition rate. The laser power was controlled through a combination of a half-wave plate and a polarizer. The pulses were focused using a 125 mm focal length plano-convex lens (PLCX-25.4-64.4-UV-670-1064) with a broadband antireflection coating covering the laser spectrum. The sample was placed on a computer-controlled 3D translation stage and translated through the beam path of the laser in order to process an area larger than the laser spot size. The number of pulses incident on the sample was controlled by adjusting the translation speed of the sample.

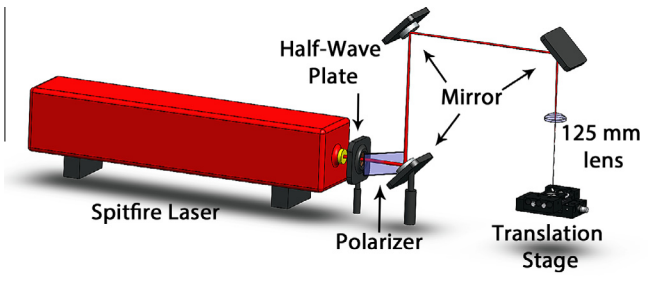

Fig. 1. Schematic of the femtosecond laser surface processing (FLSP) used in present study.

The defining physical characteristics for the samples analyzed in the present study as well as the laser parameters used in fabrication are summarized in Table 1 scanning electron microscope (SEM) images and 3D profiles of the samples are shown in Fig. 2. The 3D profiles of the sample surfaces were generated using a 3D confocal laser scanning microscope (Keyence VK-X200). The Peak to Valley Height, RMS surface roughness, and Surface Area Ratio (total area of the microstructures divided by the projected area) are measured with the Keyence instrument. The separation between the microstructures is determined by a 2D Fast Fourier Transform analysis of the SEM image.

The control sample in the present study was 304 stainless steel polished to a mirror finish through the use of a series of buffing compounds. As can be seen from Fig. 2, the FLSP samples have mound like microstructures surrounded by deep valleys. Although it cannot be seen from the SEM images in Fig. 2, the mound like microstructures are covered in a layer of nanoparticles [23,28]. Samples S1–S3 are a series created with varying laser fluence but constant shot number (N = 840). The surface structures are Below Surface Growth (BSG) Mounds as described in Ref. [21]. A visual inspection of Fig. 2 demonstrates that the microscale structures in this series are similar in shape, but increase in size and separation. Quantitative analysis shows that these samples all have roughly equivalent surface area ratios, but have concurrently increasing peak-to-valley height, RMS surface roughness, and microstructure separation. Sample S4 was fabricated with a higher laser fluence in order to generate Above Surface Growth (ASG) Mounds [21]; this sample is characterized by taller, narrower microstructures surrounded by circular pits.

It is well known that the wetting and the wicking ability of a surface greatly affects its heat transfer performance. The FLSP process has a significant impact on the wetting and wicking ability of the surface. A Ramé-Hart Model 590 F4 Series Goniometer and Tensiometer was used to measure the contact angle of both the polished and processed samples using deionized water. The contact angle of the polished surface was found to be approximately 80° while FLSP surfaces all had contact angles of nearly zero. When a small droplet is placed on each of the surfaces, the droplet is absorbed in its entirety into the surface in a very fast manner. The surfaces are considered superwicking because the wetting front easily spreads across the entire surface in a matter of a few seconds as confirmed by flow visualization using a high speed camera. The superwicking behavior is attributed to the presence of the porous layer of nanoparticles that induces high capillary wicking actions

2.2. Pool boiling experimental setup and procedure

A closed system pool boiling experimental setup was used for the heat transfer experiments. This setup is highlighted in Fig. 3. The experimental setup was designed to accommodate a variety of working fluids. For the presented results, the test rig was filled with eight liters of deionized water. The system was brought to

Table 1
Physical characteristics of the 304 stainless steel analyzed samples.

Sample	Peak to valley height (μm)	Surface roughness (μm)	Surface area ratio	Separation (μm)	CHF (W/cm^2)	Superheat (C°)
S1	7.1	1.4	3.85	6.0	142	29.2
S2	22.3	4.6	3.79	15.9	121	22.2
S3	31.3	7.8	3.82	26.1	110	22.8
S4	35.8	7.4	4.7	20.1	122	18.1

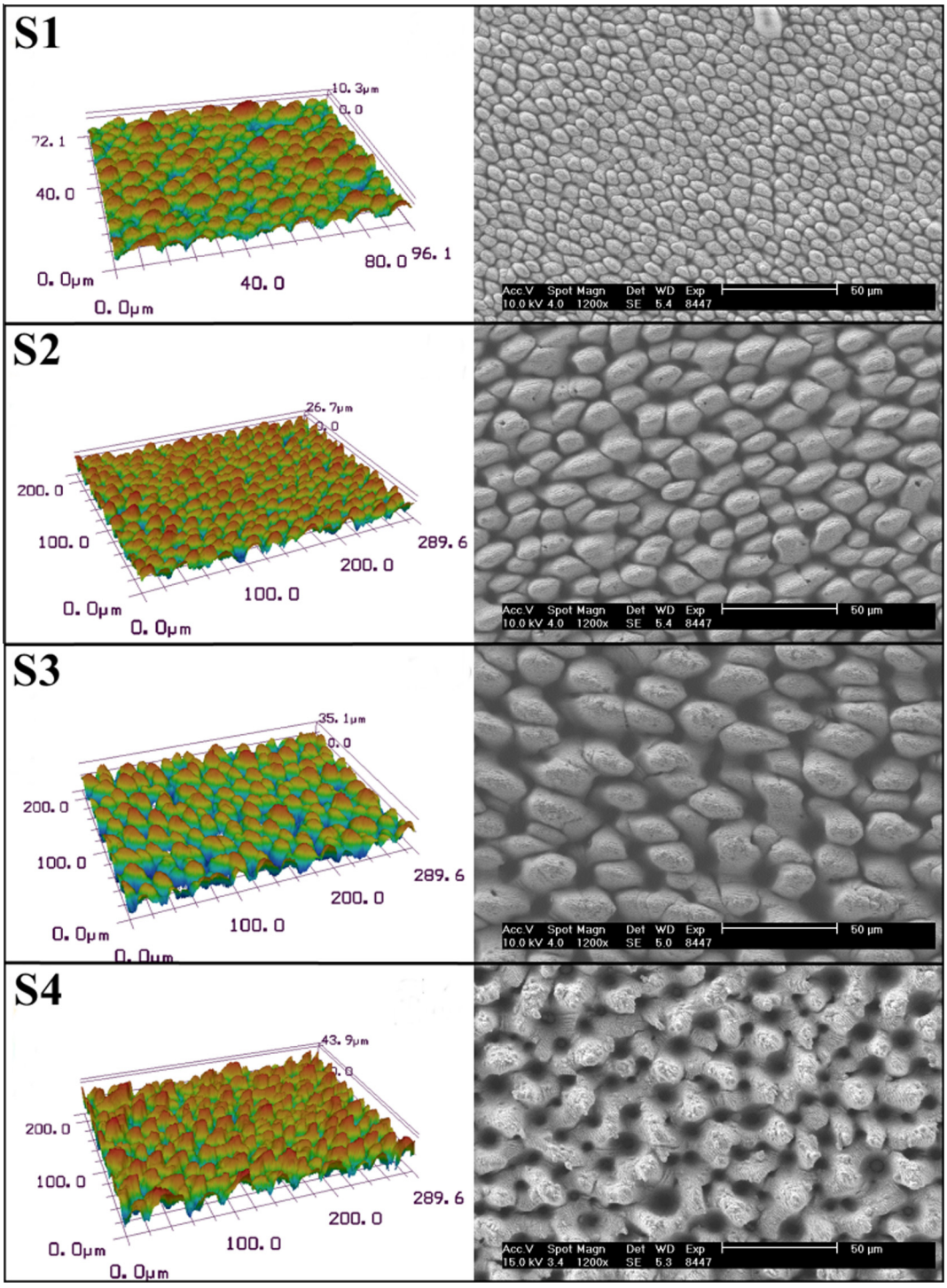

Fig. 2. SEM and laser confocal microscope images of the femtosecond laser processed surfaces. Left – confocal microscope 3D profile, right – SEM images.

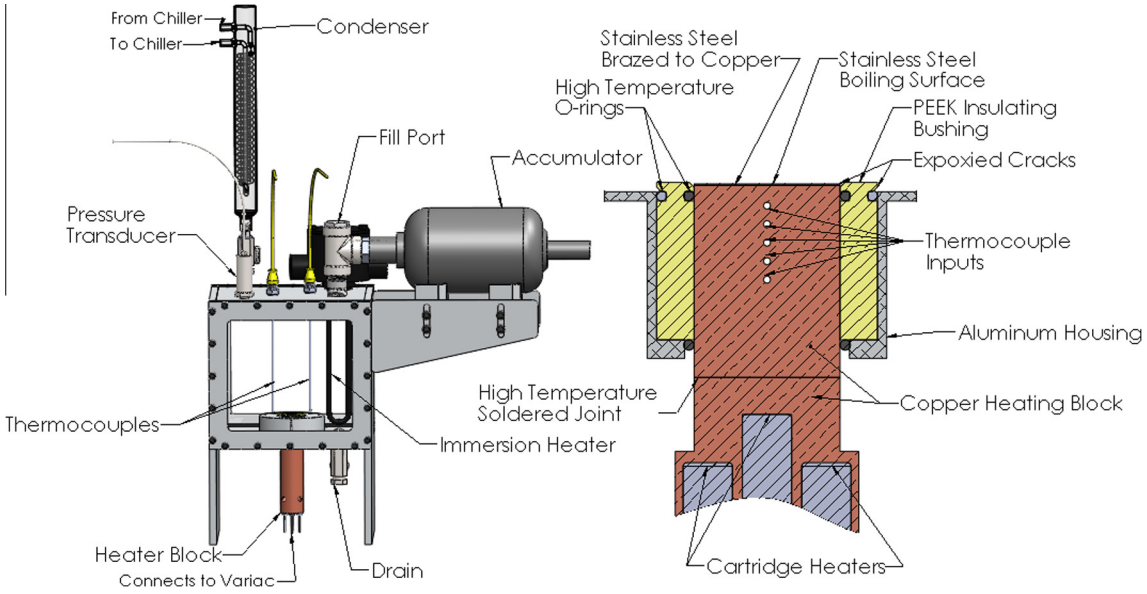

Fig. 3. Left – full experimental pool boiling setup, right – cross sectional view of heating block and boiling surface.

the saturation temperature of the water at atmospheric pressure by the use of an immersion heater (Omega – MT-112E2/120V) controlled by an analog variac. The water temperature and internal pressure were monitored with the use of two K-type thermocouples (Omega – M12KIN-18-U-6-D) and a pressure transducer (Omega – MMA100V5P4C0T4A5CE) connected to a National Instrument Data Acquisition Board. The water was degassed for a half hour before measurements were taken; the evaporated water was directed through a coil condenser (Quark Glass – qc-6-4sp) and noncondensable gases were vented to the atmosphere. The condenser was supplied with cold water with the use of a chiller. The experimental setup also includes a bladder accumulator for regulating the overall system pressure. This feature of the boiling rig was not used for the present experiment as all measurements were taken at atmospheric pressure. Two Lexan view windows were incorporated into the test rig to allow for flow visualization.

Once the system was allowed to reach the saturation temperature of the water, power to the heater was gradually increased using a copper heating block containing five cartridge heaters (Omega – CSH-203450/120V) controlled with an analog variac. This copper heating block was attached to the upper copper heating block (see Fig. 3) with the use of a high temperature solder (McMaster – 7685A12). The upper copper heating block has five thermocouple holes drilled to the center of the block. The thermocouples (located 3.18 mm apart) were used to measure the temperature gradient within the block and to calculate the heat flux. Heat flux values were recorded after the system had reached steady state monitored through an in-house LabVIEW program. The test section consists of a 25.4 mm diameter and .254 mm thick 304 stainless steel disk. The size of the test section was chosen to be sufficiently large in order to eliminate any heater size effects on the critical heat flux. This was done by determining the Bond number for the given heater size. This number gives a ratio of heater size to bubble departure size. A test sample is considered to be sufficiently large if the Bond number is greater than 3 [29]. The Bond number is calculated using Eq. (1):

$$Bo = \frac{g(\rho_l - \rho_v)}{\sigma} D^2 \tag{1}$$

where g is the acceleration due to gravity, ρ_l and ρ_v are the liquid and vapor densities respectively, σ is the surface tension of the liquid in air, and D is the diameter of the heater surface. Using this equation, the Bond number was found to be around 100; therefore it can be assumed that the heater size can be neglected. The stainless steel test section thickness was chosen to minimize the operating temperatures of the heating block at high heat fluxes. The test section was brazed onto the copper heating block using a silver solder paste (Muggyweld – SSQ-6) to ensure an efficient contact between the two. The surface temperature of the test section was obtained with the use of the measured temperature gradient along the heating block. The contact resistance between the copper and stainless steel was neglected due to the very thin and the highly conductive silver solder braze used. A high temperature PEEK plastic insulating bushing was used to insulate the upper copper heating block. Fiberglass insulation (not shown in Fig. 3) was used to insulate the lower copper heating block. High temperature silicon o-rings were used to seal between the concentric heating and insulating pieces. To ensure that nucleation would not prematurely occur on the outer edges of the boiling surface, a special epoxy (Mcmaster – 7513A1) was used for bonding dissimilar materials.

2.3. Heat flux and uncertainty calculation

The five equally spaced thermocouples located in the upper heating block were used to measure the temperature gradient along the axis of the heating block and calculate the heat flux. The heat flux was calculated as:

$$q'' = k_c \frac{T_i - T_j}{x} \tag{2}$$

where k_c is the thermal conductivity of the copper, T_i and T_j are the thermocouple temperatures and x is the thermocouple separation distance. The heat flux is calculated between alternating thermocouple locations. To clarify, if the thermocouples are labeled in order from 1 to 5, the heat flux is calculated between temperatures 1 and 3, 3 and 5, 2 and 4, and then 1 and 5. This increase in separation distance reduces the uncertainty of the calculation. The minimum value of x is 6.35 mm. The thermal conductivity of copper was taken to be constant at a value of 401 W/m K. The temperature gradient and heat flux were measured at the four locations and then averaged. The critical heat flux is determined when the monitored

thermocouple temperatures spike on the order of 100 °C and burnout occurs.

Radial heat losses were minimized by insulating the copper heating blocks. The upper heating block was insulated with a PEEK plastic bushing (k_p = .25 W/m K) with a thickness of .635 cm. The lower heating block was insulated with fiberglass insulation. The thermocouple measurements were used to show that the upper copper heating block was well insulated and at uniform temperature in the radial direction. The radial heat loss can be estimated across the PEEK bushing if the aluminum housing (see Fig. 3) is assumed to be at 100 °C since it is in contact with the saturated water. At heat fluxes near the critical heat flux, the maximum temperature in the upper copper heating block was measured to be 216 °C. It is assumed that the copper/PEEK interface is at approximately 216 °C due to the highly conductive nature of the upper copper heating block; hence the radial heat loss can be estimated by Eq. (3):

$$q''r = k_p \frac{T_i - T_w}{r_p} \tag{3}$$

where k_p is the PEEK thermal conductivity, r_p is the PEEK thickness, T_w is the aluminum temperature at the wall, and T_i is the interface temperature. It was found that this heat flux is approximately 0.5 W/cm^2 which is less than 1% of the total heat flux measured at the critical heat flux. This approximation was also validated using a full 3D finite element analysis of the heating block, test surface, and insulation assembly. The boundary conditions for the simulation are as follows: convective heat transfer coefficient of 23,000 W/m^2 K at the boiling surface, heat flux of 92 W/cm^2 at the junction of the upper and lower copper heating blocks, a constant temperature of 100 °C at the PEEK/water and aluminum housing/water interface, and a natural convection coefficient of 10 W/m^2 K at the lower part of the aluminum housing (see Fig. 3). The simulation results were in excellent agreement with the theoretical approximation obtained by Eq. (3).

Uncertainties on the heat flux values as well as the surface temperatures were calculated using the standard error propagation equation. The standard deviation of the heat flux based on the accuracies of the measurement equipment is given as follows:

$$\Delta q'' = \sqrt{\left(\frac{\partial q''}{\partial x}\Delta x\right)^2 + \left(\frac{\partial q''}{\partial T_1}\Delta T\right)^2 + \left(\frac{\partial q''}{\partial T_2}\Delta T\right)^2} \tag{4}$$

The variation of the thermocouple separation (Δx) is .08 mm and the thermocouple variation (ΔT) is 1 °C. This leads to an estimated error of approximately 7.5% at an average critical heat flux.

The surface temperature was calculated from the measured heat flux. This calculation considered both the copper material as well as the stainless steel wafer. The contact between the two materials was assumed to be ideal due to the highly conductive and very thin layer of silver braze used to join the two. The surface temperature was therefore calculated as follows:

$$T_s = T_1 - \frac{q'' x_1}{k_c} - \frac{q'' x_{ss}}{k_{ss}} \tag{5}$$

where T_1 is the thermocouple temperature located closest to the surface, x_1 is the distance between T_1 and the bottom of the stainless steel wafer, x_{ss} is the stainless steel wafer thickness, and k_c and k_{ss} are the copper and stainless steel thermal conductivities respectively, allowing for variation with temperature. The estimated error for the surface temperature can be determined using the following equation:

$$\Delta T_s = \sqrt{\left(\frac{\partial T_s}{\partial T_1}\Delta T\right)^2 + \left(\frac{\partial T_s}{\partial q''}\Delta q''\right)^2 + \left(\frac{\partial T_s}{\partial x_1}\Delta x_1\right)^2 + \left(\frac{\partial T_s}{\partial x_{ss}\Delta x_{ss}}\right)^2} \tag{6}$$

Δx_1 , the variation of x_1, is 0.07 mm and Δx_{ss} the variation of the wafer thickness is 0.003 mm. With these variations the error in the surface superheat temperature calculation at the critical heat flux is around 6–13% depending on the surface.

In a similar fashion, the uncertainty of the heat transfer coefficients can also be determined using the extreme cases of the heat flux and surface temperature uncertainties. Using the standard error propagation method, uncertainties of the heat transfer coefficient range from 11% to 16% depending on the test surfaces.

3. Results and discussion

For each of the sample surfaces tested, measurements were first taken at low heat fluxes and then the heat flux was gradually increased until critical heat flux was reached. The results are shown in Fig. 4. It can be seen from this figure that there was a drastic difference between the processed and unprocessed surfaces in their heat transfer performance. The processed surfaces consistently outperformed the polished sample at every surface temperature. The polished sample was found to have a critical heat flux of 91 W/cm^2 at a surface superheat of 40 °C. This result closely matches the results found in the literature for a similar smooth metallic surface [13,30,31], as well as critical heat flux correlations [32] such as Zuber's and Kandlikar's. Zuber's model is given in Eq. (7) and Kandlikar's model is given in Eq. (8):

$$q_c = K h_{fg} \rho_v \left[\frac{\sigma g(\rho_L - \rho_v)}{\rho_v^2}\right]^{1/4} \tag{7}$$

$$q_c = h_{fg} \rho_v^{.5} \left(\frac{1+\cos\beta}{16}\right)\left[\frac{2}{\pi} + \frac{\pi}{4}(1+\cos\beta)\right]^{1/2} x[\sigma g(\rho_L - \rho_v)]^{1/4} \tag{8}$$

The value of the constant K is .131 as determined by Zuber. The terms h_fg, ρ_v, ρ_L, σ, and g are the latent heat of vaporization, the vapor density, the liquid density, the surface tension, and gravity. These properties are evaluated for water at 100 °C. The β term in Eq. (8) is the receding contact angle for the polished stainless steel surface which was measured to be 70°. Zuber's equation predicts a critical heat flux of about 110 W/cm^2; this prediction overestimates the measured result for the polished sample in the present experiments. This discrepancy can be attributed to the fact that Zuber's model does not take into account the surface wettability which we know has significant effects on the critical heat flux. Using Kandlikar's model, the critical heat flux was predicted to be 91.7 W/cm^2 and agreed extremely well with our measured value.

The reported critical heat flux of the polished sample agrees well with theory and other values found in the literature, but there is a variation in the surface temperature reported. The polished sample in our work was found to have a wall superheat temperature of 40 °C at the critical heat flux. In various published data [13,30,31] the wall superheat temperature has been shown to range from 10 °C to 55 °C. Even though all the above referenced experiments had Bond numbers greater than 3, they significantly differ in heater thickness. It has been reported that heater thickness and thermal conductivity can have an effect on the heat transfer coefficient [33,34]. The differences in wall superheat between the present experiments and published literature could therefore be likely due to variances in heater thickness.

The maximum CHF observed was with sample S1 which had a CHF of 142 W/cm^2. All processed surfaces had consistently higher CHF values than the polished sample. An overview of the boiling performance for each test sample is given in Table 2.

Although the four processed samples had the same contact angle, there is a significant difference between the samples which can no longer be related to a change in the contact angle. It is well

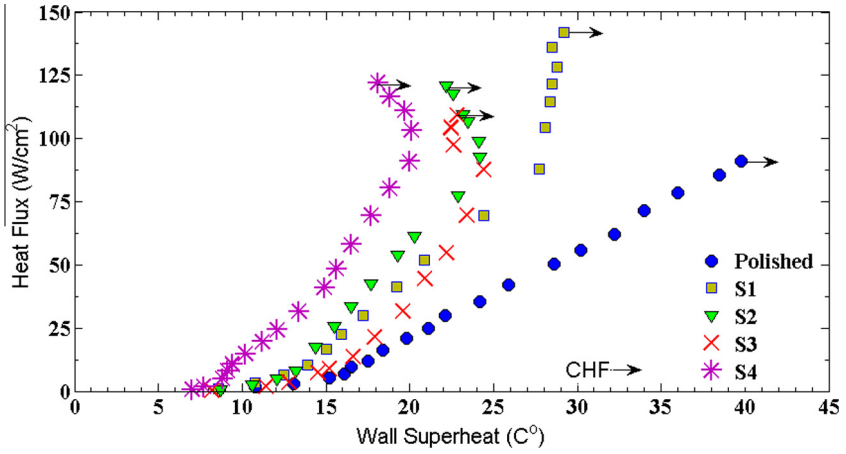

Fig. 4. Heat fluxes with respect to surface superheat for both the laser processed and polished stainless steel surfaces.

Table 2
Summary of boiling performance for each test surface.

Sample	CHF (W/cm^2)	CHF surface superheat (°C)	Onset of nucleate boiling superheat (°C)	Maximum heat transfer coefficient (W/m^2 –K)
Polished	91	39.8	10.8	22,900
S1	142	29.2	8.6	48,600
S2	118	22.6	8.7	52,200
S3	109	22.8	8.2	47,800
S4	122	18.1	7	67,400

known that reducing the contact angle to zero does not result in reaching a limit on critical heat flux enhancement and that additional mechanisms become dominant. As can be seen from Table 2 and Fig. 4, there is a definite trend in CHF enhancement for samples S1–S3. For these surfaces the surface area ratio is nearly constant but the critical heat flux increases with decreasing structure height and spacing. The reason for this increase in CHF for these samples can be related to the microstructure geometry. As can be seen from Fig. 2, the area between the microstructures increases from S1 to S3. For S1 the mound structures are densely packed and narrow channels or cracks are formed between microstructures. This network of channels, in addition to the nanoparticle layer on the microstructures, allows for high capillary wicking effects which help to quickly replenish the heated surface with cold liquid after local evaporation occurs and consequently delay the critical heat flux. As the sample number increases, the separation and size of the microstructures also increase; this results in the formation of deep pits in between the microstructures instead of the channels. These deep pits and holes reduce the wicking potential of the surfaces and the wicking effect is mainly dominated by the presence of the layer of nanoparticles covering the mound structures.

As mentioned earlier, sample S4 is slightly different than the other samples. However, its critical heat flux enhancement can still be explained by the same approach. S4 resulted in the second highest CHF of 122 W/cm^2 observed, however had a larger peak-to-valley height as well as structure spacing. The most notable geometric difference between S4 and the rest is the surface area ratio as its surface area ratio is significantly higher than the other samples. This increase in the surface area ratio is the reason for the increase in critical heat flux over sample S2 which had a much denser microstructure arrangement. The larger surface area ratio results in more surface area in contact with the liquid and thus can compensate for a lack of wicking ability due to the larger microstructure spacing. The increase in surface area ratio can also result in a better wetting surface as described by the classic Wenzel model for a droplet on a rough surface. The contact angle measurements taken were not able to prove a difference in wettability between the processed surfaces due to the highly wicking nature of the processed surfaces and the limits of the measuring device. Hence, S4 has higher CHF than S2 and S3 because of its relatively higher wettability. It can be therefore concluded from the observed results, that the enhancement in CHF is due to a combination of both surface wettability and capillary wicking.

The local maximum superheat temperature that arises in S2–S4 can be related to the thermal conductivity of the surface and the active nucleation site density. Since the thermal conductivity of stainless steel is relatively low compared to other metals such as copper, local sites with different heat fluxes can occur [33]. As the number of active nucleation sites increase the average surface temperature would then decrease. Because the processed surfaces have roughness on both the nano and microscale, there is a wide range of potential nucleation sites that could be activated at high heat fluxes. Near the critical heat flux, the maximum amount of nucleation sites is active and thus reduces the surface temperature. The polished sample does not have this nano and microscale roughness so there are no additional nucleation sites to activate at high heat fluxes and thus the curve remains nearly linear.

The shift of the boiling curves to the left with the processed surfaces is very advantageous to heat transfer applications as it corresponds to an enhancement of the heat transfer coefficients and allows for a large amount of heat to be transferred at relatively low surface temperatures. The steep slope of the curve is also advantageous because of the relatively small surface temperature change (around 10 °C for S4). For all processed surfaces investigated, significant enhancement of the heat transfer coefficients were observed in comparison to the polished surface.

Heat transfer coefficients based on the projected area were determined for each of the test samples and plotted in Fig. 5. A summary of the maximum heat transfer coefficients is also given in Table 2. The maximum heat transfer coefficient values varied from 22,900 to 67,400 W/m^2 K. As expected for nucleate boiling, the heat transfer coefficients increase with increasing heat flux.

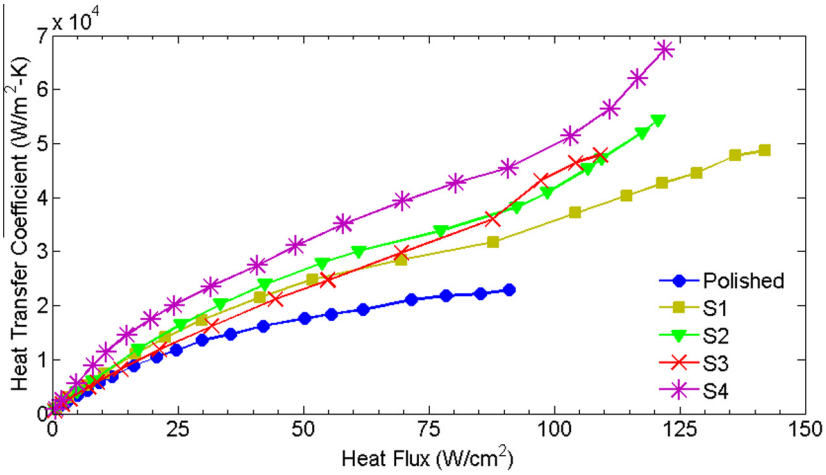

Fig. 5. Heat transfer coefficient with respect to wall heat flux for each sample surface.

The shape of each curve looks nearly the same for heat flux values up to 90 W/cm^2. Beyond this point the slope of the curve for the processed samples changes significantly. This change in slope is a result of the additional nucleation sites which become active at higher heat fluxes (e.g., smaller radius cavities); the probability of active nucleation sites in this region is expected to be different for each test sample.

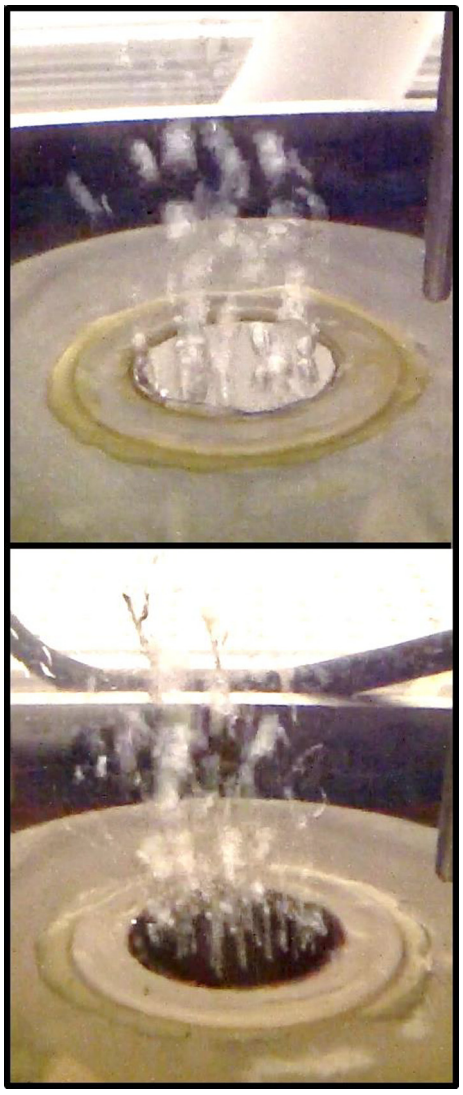

Fig. 6. Near onset of nucleate boiling: top – polished sample, 13 °C superheat and 3 W/cm^2, bottom – S4, 7.7 °C and 2 W/cm^2.

Samples S1–S3 have very similar heat transfer coefficient curves. This is expected since these surfaces have nearly identical surface area ratios. The curves of S1–S3 diverge at around 90 W/cm^2. Beyond this point the heat transfer coefficients follow the trend of increasing microstructure peak-to-valley height. The microstructures act like cooling fins for heat to be conducted through. As the height of the microstructures increase, the more efficiently the surface is cooled and thus increases the heat transfer coefficient. Sample S4 consistently has higher heat transfer coefficients than all the other samples. The overall enhancement of the heat transfer coefficients can be attributed to efficient nucleate boiling and an increase in the surface area ratio. The increase in the slope beyond the divergent point (at 90 W/cm^2) can also be related to the microstructure peak-to-valley height. As the height is increased the change in slope is also increased. The enhancement of the heat transfer coefficients at high heat fluxes is due to a combination of the tall nature of the microstructures [33] and the higher surface area ratio, as well as a higher probability of finding a nucleation site which can be activated at higher heat fluxes.

As for the Onset of Nucleate Boiling (ONB), it can be seen from Fig. 4 and Table 2 that the ONB occurred at much lower wall superheat values for the processed surfaces when compared to the polished surface. This is due to the nano and microscale features present on the processed surfaces which allow for nucleation sites that activate with less energy. Fig. 6 shows the difference in nucleation between S4 and the polished surface at low heat fluxes further supporting the above mentioned statement. As can be seen from Fig. 6, sample S4 has a much higher nucleation site density and produces much smaller bubbles that quickly detach from the surface compared to the polished sample. This difference in bubble size and departure rate and diameter also occurred at higher heat fluxes and surface temperatures. Sample S4 was found to have the smallest ONB at around 7 °C compared to about 10 °C for the polished sample.

4. Conclusions

Through the use of femtosecond laser surface processing (FLSP), functionalized stainless steel surfaces were fabricated with hierarchical micro/nanostructures. The structures consist of mound like microstructures covered by a dense layer of nanoparticles resulting in highly wetting and superwicking surfaces with augmented surface area and increased nucleation site density. Pool boiling heat

transfer experimental results revealed that using the laser processed stainless steel surfaces, the critical heat flux can be increased from 91 to 142 W/cm^2 while also increasing the maximum heat transfer coefficients from 23,000 to 67,400 W/m^2 K. Increase in the critical heat flux has been attributed to increase in surface wettability and wicking capabilities. Processed surfaces with tightly packed mound structures resulted in better wettability and wicking and thus resulted in higher critical heat fluxes. The enhancement in heat transfer coefficients are related to the surface area ratio, structure height, and the active nucleation site density. It was found that the higher the surface area ratio the higher the heat transfer coefficients. It was also found that microstructure peak-to-valley height can result in a cooling fin effect and further increase the heat transfer coefficients at high heat fluxes. The heat transfer enhancement at low heat fluxes can be attributed to the increase in nucleation site density and more efficient bubble departure dynamics.

Conflict of interest

None declared.

Acknowledgment

This work has been supported by a grant through the Nebraska Center for Energy Sciences Research (NCESR) with funds provided by Nebraska Public Power District (NPPD) to the University of Nebraska – Lincoln (UNL) No. 4200000844, a NASA EPSCoR Grant # -NNX13AB17A and by funds from the Department of Mechanical and Materials Engineering and the College of Engineering at UNL, awarded to SN.

References

[1] S. Ndao, Y. Peles, M.K. Jensen, Experimental investigation of flow boiling heat transfer of jet impingement on smooth and micro structured surfaces, Int. J. Heat Mass Transfer 55 (19–20) (2012) 5093–5101.
[2] S. Kim, H.D. Kim, H. Kim, H.S. Ahn, H. Jo, J. Kim, M.H. Kim, Effects of nano-fluid and surfaces with nano structure on the increase of CHF, Exp. Therm. Fluid Sci. 34 (4) (2010) 487–495.
[3] K.-H. Chu, R. Enright, E.N. Wang, Structured surfaces for enhanced pool boiling heat transfer, Appl. Phys. Lett. 100 (24) (2012) 241603.
[4] M. Rahman, S.M. King, E. Olceroglu, M. Mccarthy, Nucleate boiling on biotemplated nanostructured surfaces, in: ASME 2012 International Mechanical Engineering Congress and Exposition, American Society of Mechanical Engineers, 2012, pp. 2801–2808.
[5] Z. Yao, Y.-W. Lu, S.G. Kandlikar, Micro/nano hierarchical structure in microchannel heat sink for boiling enhancement, in: 2012 IEEE 25th International Conference on Micro Electro Mechanical Systems (MEMS), 2012, pp. 285–288.
[6] A.R. Betz, J. Jenkins, C.-J. Cj Kim, D. Attinger, Boiling heat transfer on superhydrophilic superhydrophobic and superbiphilic surfaces, Int. J. Heat Mass Transfer 57 (2) (2013) 733–741.
[7] A.R. Betz, J. Xu, H. Qiu, D. Attinger, Do surfaces with mixed hydrophilic and hydrophobic areas enhance pool boiling?, Appl Phys. Lett. 97 (14) (2010) 141909.
[8] H. Jo, H.S. Ahn, S. Kang, M.H. Kim, A study of nucleate boiling heat transfer on hydrophilic, hydrophobic and heterogeneous wetting surfaces, Int. J. Heat Mass Transfer 54 (25–26) (2011) 5643–5652.
[9] H.T. Phan, N. Caney, P. Marty, S. Colasson, J. Gavillet, Surface wettability control by nanocoating: the effects on pool boiling heat transfer and nucleation mechanism, Int. J. Heat Mass Transfer 52 (23–24) (2009) 5459–5471.
[10] Z. Yao, Y.-W. Lu, S.G. Kandlikar, Effects of nanowire height on pool boiling performance of water on silicon chips, Int. J. Therm. Sci. 50 (11) (2011) 2084–2090.
[11] M.-C. Lu, R. Chen, V. Srinivasan, V.P. Carey, A. Majumdar, Critical heat flux of pool boiling on si nanowire array-coated surfaces, Int. J. Heat Mass Transfer 54 (25–26) (2011) 5359–5367.
[12] R. Chen, M.-C. Lu, V. Srinivasan, Z. Wang, H.H. Cho, A. Majumdar, Nanowires for enhanced boiling heat transfer, Nano Lett. 9 (2) (2009) 548–553.
[13] H.S. Ahn, C. Lee, H. Kim, H. Jo, S. Kang, J. Kim, J. Shin, M.H. Kim, Pool boiling CHF enhancement by micro/nanoscale modification of zircaloy-4 surface, Nucl. Eng. Des. 240 (10) (2010) 3350–3360.
[14] H.S. Ahn, C. Lee, J. Kim, M.H. Kim, The effect of capillary wicking action of micro/nano structures on pool boiling critical heat flux, Int. J. Heat Mass Transfer 55 (1–3) (2012) 89–92.
[15] B. Feng, K. Weaver, G.P. Peterson, Enhancement of critical heat flux in pool boiling using atomic layer deposition of alumina, Appl. Phys. Lett. 100 (5) (2012) 053120.
[16] T.J. Hendricks, S. Krishnan, C. Choi, C.-H. Chang, B. Paul, Enhancement of pool-boiling heat transfer using nanostructured surfaces on aluminum and copper, Int. J. Heat Mass Transfer 53 (15–16) (2010) 3357–3365.
[17] C. Young Lee, M.M. Hossain Bhuiya, K.J. Kim, Pool boiling heat transfer with nano-porous surface, Int. J. Heat Mass Transfer 53 (19–20) (2010) 4274–4279.
[18] J.P. McHale, S.V. Garimella, T.S. Fisher, G.A. Powell, Pool boiling performance comparison of smooth and sintered copper surfaces with and without carbon nanotubes, Nanoscale Microscale Thermophys. Eng. 15 (3) (2011) 133–150.
[19] C. Li, Z. Wang, P.-I. Wang, Y. Peles, N. Koratkar, G.P. Peterson, Nanostructured copper interfaces for enhanced boiling, Small 4 (8) (2008) 1084–1088.
[20] C. Zuhlke, T. Anderson, D. Alexander, Formation of multiscale surface structures on nickel via above surface growth and below surface growth mechanisms using femtosecond laser pulses, Opt. Express 21 (7) (2013) 97–98.
[21] C.A. Zuhlke, T.P. Anderson, D.R. Alexander, Formation of multiscale surface structures on nickel via above surface growth and below surface growth mechanisms using femtosecond laser pulses, Opt. Express 21 (7) (2013) 8460–8473.
[22] C.A. Zuhlke, T.P. Anderson, D.R. Alexander, Comparison of the structural and chemical composition of two unique micro/nanostructures produced by femtosecond laser interactions on nickel, Appl. Phys. Lett. 103 (12) (2013) 121603.
[23] C.A. Zuhlke, T.P. Anderson, D.R. Alexander, Fundamentals of layered nanoparticle covered pyramidal structures formed on nickel during femtosecond laser surface interactions, Appl. Surf. Sci. 21 (7) (2013) 8460–8473.
[24] C.A. Zuhlke, D.R. Alexander, J.C. Bruce, N.J. Ianno, C. a Kamler, W. Yang, Self assembled nanoparticle aggregates from line focused femtosecond laser ablation, Opt. Express 18 (5) (2010) 4329–4339.
[25] A.Y. Vorobyev, C. Guo, Direct femtosecond laser surface nano/microstructuring and its applications, Laser Photon. Rev. 7 (3) (2013) 385–407.
[26] B.K. Nayak, M.C. Gupta, Ultrafast laser-induced self-organized conical micro/nano surface structures and their origin, Opt. Lasers Eng. 48 (10) (2010) 966–973.
[27] E. Stratakis, A. Ranella, C. Fotakis, Biomimetic micro/nanostructured functional surfaces for microfluidic and tissue engineering applications, Biomicrofluidics 5 (1) (2011).
[28] C. Kruse, T. Anderson, C. Wilson, C. Zuhlke, D. Alexander, G. Gogos, S. Ndao, Extraordinary shifts of the Leidenfrost temperature from multiscale micro/nanostructured surfaces, Langmuir 29 (31) (2013) 9798–9806.
[29] J. Kim, J.F. Benton, D. Wisniewski, Pool boiling heat transfer on small heaters: effect of gravity and subcooling, Int. J. Heat Mass Transfer 45 (19) (2002) 3919–3932.
[30] D. Wen, Y. Ding, Experimental investigation into the pool boiling heat transfer of aqueous based γ-alumina nanofluids, J. Nanopart. Res. 7 (2–3) (2005) 265–274.
[31] R.J. Benjamin, A.R. Balakrishnan, Nucleation site density in pool boiling of saturated pure liquids: effect of surface microroughness and surface and liquid physical properties, Exp. Therm. Fluid Sci. 15 (1) (1997) 32–42.
[32] S.G. Kandlikar, A theoretical model to predict pool boiling CHF incorporating effects of contact angle and orientation, J. Heat Transfer 123 (6) (2001) 1071.
[33] I.L. Pioro, W. Rohsenow, S.S. Doerffer, Nucleate pool-boiling heat transfer. I: Review of parametric effects of boiling surface, Int. J. Heat Mass Transfer 47 (23) (2004) 5033–5044.
[34] T.L. Chuck, J.E. Myers, The effect of heater plate thickness on boiling heat-transfer coefficients, Int. J. Heat Mass Transfer 21 (2) (1978) 187–191.